



Comparison of STIS CCD CTI Corrections on Photometry

L. Prichard¹

¹ Space Telescope Science Institute, Baltimore, MD

12 May 2022

ABSTRACT

The STIS CCD detector suffers from charge transfer inefficiency (CTI) which can be corrected for using a pixel-based or empirical flux correction ($CTI = 1 - CTE$). Here we present a comparison of these two CTI correction methods and compare these to the magnitudes derived from non-CTI corrected CCD images. We use data spanning 2010 to 2022 and derive photometry for the same sources for each CTI method to compare the magnitudes. We explore the absolute differences between the CTI corrected magnitudes, and their spatial, time and magnitude dependence. The offsets are smallest for the brightest stars and deviate further from zero with increasing magnitude (< 18 mag: 0.020 mag, 0.12%; 18–19 mag: 0.037 mag, 0.20%; 19–22 mag: -0.084 mag, -0.35%). Stars brighter than 19 mag are marginally over-corrected with both CTI methods. Stars fainter than 19 mag are slightly under-corrected by the pixel-based CTI method and slightly over-corrected with the empirical flux CTI method. Generally, we find that the offsets between the codes are small ($< 1\%$), consistent with past results, and well within the quoted $\sim 5\%$ STIS photometric errors.

Contents

1. Introduction	2
2. Data	3
2.1 Observations	3

2.2 CCD CTI Corrections	3
2.3 Image Alignment	4
3. Analysis	5
3.1 Source Detection & Catalogs	5
3.2 PSF Creation	5
3.3 Photometry	7
4. Results	8
4.1 CTI Corrected Magnitude Comparison	8
4.2 Spatial Dependence of Outliers	10
4.3 Time Dependence	11
4.4 Magnitude Dependence	14
5. Discussion	16
5.1 Differences Between This Work and ISR 2015-04	16
5.2 Comparison of Results	17
6. Summary & Conclusions	18
Acknowledgments	19
References	20
Appendix A	20
Future Work: Improving CTI Time Dependence Parameters	20
Appendix B	22

1. Introduction

The Space Telescope Imaging Spectrograph (STIS) instrument on the *Hubble Space Telescope* (HST) has three detectors, including one charge-coupled device (CCD). Photons land on the CCD and are converted to charge which is then transferred across the array to the ‘readout’, first in the slow parallel direction and then in the fast serial direction. This transfer of charge is not efficient and therefore a charge transfer inefficiency (CTI) correction is required to minimize CTI effects on the data. The detector is also subject to time-dependent sensitivity (TDS) effects as it ages. In addition, the CTI worsens with time as the detector is exposed to radiation during orbit.

CTI corrections are not applied by default in the standard CALSTIS pipeline for STIS imaging. The choice of correction method is up to the user and there are currently two ways to correct for the effects of CTI on STIS CCD images. The first is a pixel-based correction (based on the work of Anderson & Bedin, 2010), where the CTI effects of the detector are modeled and removed directly from the images themselves. This type of method is also applied to the other HST instruments as standard and it is considered the most flexible correction as it can be applied to images even if they have extended and complex structures. The other method is an empirical flux correction (based on equations from Goudfrooij et al., 2006) where the magnitude of a source is measured from non-CTI corrected images and a CTI correction to the magnitude is derived. This empirical flux CTI correction is applied to STIS CCD spectra in the HSTCAL CALSTIS

pipeline with the CTECORR algorithm but not to imaging. The correction is applied during the spectral extraction phase using parameters defined in the CCDTAB reference file.

In this work, we compare the photometric performance of the two STIS CTI correction methods and discuss the benefits and shortfalls of each. A similar comparison of the photometric performance was performed in STIS Instrument Science Report (ISR) 2015-04 (Biretta et al., 2015b) which we refer back to for a comparison of the results derived here. However, there are some important differences between the studies that we cover when comparing the results. Two other ISRs comparing the CTI methods look at the astrometric accuracy (Biretta et al., 2015c, STIS ISR 2015-05) and the detector spatial and temperature CTI dependence (Biretta et al., 2015a, STIS ISR 2015-03) which we refer the reader to for more information.

We go over the data properties, including observations, CTI corrections, and image alignment in Section 2. We then detail the analysis performed on the images in Section 3 (source detection, PSF creation and photometry). This analysis includes a summary of the same methods described in the recent full-field sensitivity analysis in STIS ISR 2022-02 (Prichard, 2022a) which is an update to the work presented in STIS ISR 2013-03 (Roman-Duval & Proffitt, 2013). We then present the results, including a comparison of the CTI corrected magnitudes, and their spatial, time and magnitude dependence in Section 4. In Section 5, we compare the methods and results of this work to that of ISR 2015-04. Finally, we give an overview of this study and summarize our main results in Section 6.

2. Data

2.1 Observations

We use the CCD images used to track the full-field sensitivity of STIS (ISR 2013-02, ISR 2022-02) downloaded from MAST with ASTROQUERY (Ginsburg et al., 2019). We use only those images taken after Servicing Mission 4 (SM4) in 2009 (when STIS was repaired), as these are the only ones that can be corrected with the pixel-based CTI code at present (see Section 2.2). The CCD observations are of the standard star field NCG 5139 taken yearly between 2010 and 2022. All the images are taken with the unfiltered 50CCD aperture, on default science amplifier D, and with $\text{CCDGAIN} = 4$ to minimize saturation. The images have mostly 10 s and 60 s total exposure times with 2 s and 30 s per read, respectively, and the same position angles (PAs). See Table 1 for a summary of the images used in this analysis and their properties. The CCD data were calibrated, cosmic-ray rejected and distortion corrected (sx2.fits files).

2.2 CCD CTI Corrections

For the CTI method comparison, we apply the two different CTI correction codes at different stages of the analysis. The new pixel-based CTI correction method is run with

the STIS_CTI code¹ and produces fully-calibrated CTI corrected images (s2c.fits) ready for analysis. This code is based on the work of Anderson & Bedin, 2010 with parameters calibrated to STIS data (work done by Lockwood et al., see ISR 2015-04 and references therein).

The code for the original empirical CTI correction, CTESTIS², is available in the STISTOOLS package (previously available in IRAF as STSDAS.HST_CALIB.STIS.CTESTIS³). This code is based on the equations and work of Goudfrooij & Bohlin 2006, Goudfrooij et al. 2006. For STIS spectroscopy, this code is applied as standard in the CALSTIS pipeline for extracted spectra. For STIS imaging, users run this code to derive empirical CTI corrections for source photometry. This routine takes inputs of net counts for a source (background subtracted), a sky background estimate, and the y -position on the detector (since CTI effects worsen furthest from the readout). The sky background is measured from individual cosmic-ray split, bias- and dark-subtracted, and flat-fielded images (flt.fits) that have not had any sky subtracted. The net counts measured from the science images (sx2.fits) are then scaled to the exposure time of the split image (e.g., if CRSPLIT = 5, the counts are divided by five). The code then generates an empirical magnitude correction (Δm) to be applied to the derived source magnitude.

At present the STIS_CTI pixel-based CTI correction code is only applicable to data taken after post-SM4 on amplifier D. We therefore only use those CCD images in this analysis to directly compare the pixel-based CTI correction method ('pixbased'), empirical Δm CTI correction ('empirical') method and non-CTI corrected magnitudes ('no CTI'). For this analysis, we only use images taken at two sky background levels, corresponding to the 2 s and 30 s split exposure times. The corrections are applied to a wider range of sky backgrounds in other science data.

2.3 Image Alignment

The images were aligned using the TWEAKREG routine from the DrizzlePac package (Gonzaga et al. 2012, Hoffmann et al. 2021)⁴ and as described in ISR 2022-02. The images were aligned onto the reference image (obat01050 from proposal 11854) with an average accuracy of ~ 0.1 – 0.2 pix. Position, rotation and linear stretch information is applied to the WCS header keywords with TWEAKREG, but the STIS geometric distortion corrections remain unchanged. We successfully aligned all 65 of the CCD exposures (spanning 2010 to 2022), for both pixel-based CTI corrected and non-CTI corrected images. Tips and tricks for testing TWEAKREG parameters for STIS imaging

¹<https://www.stsci.edu/hst/instrumentation/stis/data-analysis-and-software-tools/pixel-based-cti>

²<https://stistools.readthedocs.io/en/latest/ctestis.html>

³https://github.com/iraf-community/stsdas/blob/main/stsdas/pkg/hst_calib/stis/ctestis.cl

⁴<https://drizzlepac.readthedocs.io/en/latest/index.html>

are available in a new STIS DrizzlePac Jupyter Notebook⁵.

3. Analysis

The source detection, photometry and analysis methods used for this CTI method comparison is in line with that presented in ISR 2022-02. We briefly summarize each of the analysis steps here but refer the reader to that full-field sensitivity ISR for more details.

3.1 Source Detection & Catalogs

We use the Python DAOSTARFINDER routine from the PHOTUTILS package (Bradley et al. 2020) to identify sources on the reference image. We use the pixel-based CTI corrected image for source detection then use the same source list and positions for the non-CTI corrected images for consistency. We set parameters to identify round (`roundlo=-0.25` and `roundhi=0.25`) and sharp (`sharp=0.85`) point sources. We then perform some basic cleaning to remove close pairs (within $0.8''$) and a visual inspection to remove contaminated or non-stellar objects. We identify a cleaned list of 125 sources (red) shown in Figure 1 on the pixel-based CTI corrected (top) and non-CTI corrected reference image (bottom).

We then select a subset of stars that appear in all the images for creating consistent point-spread functions (PSFs) for all the pointings. We select stars with a clear profile and no signs of saturation (as determined from the reference images), resulting in a list of 19 ‘PSF stars’.

3.2 PSF Creation

We use the PSFs for each image to determine appropriate aperture sizes to use for photometry. To create a PSF for each image, we stack the stars in the PSF list using new PSF stacking tools⁶. We extract each star and interpolate them onto a sub-pixel grid for fine alignment. The PSFs are aligned on the brightest pixel and the median is taken. We interpolate the average PSF profiles back to the native CCD pixel scale to generate one PSF per image. We fit a 2D Moffat profile (using ASTROPY models⁷, Astropy Collaboration 2013, 2018) to each PSF to determine a full-width-half-max (FWHM) value in pixels. See Table 1 for a summary of PSF FWHM values for each image.

⁵<https://github.com/spacetelescope/STIS-Notebooks>,
<https://www.stsci.edu/hst/instrumentation/stis/data-analysis-and-software-tools>

⁶https://github.com/mrevalski/hst_wfc3_psf_modeling

⁷<http://www.astropy.org>

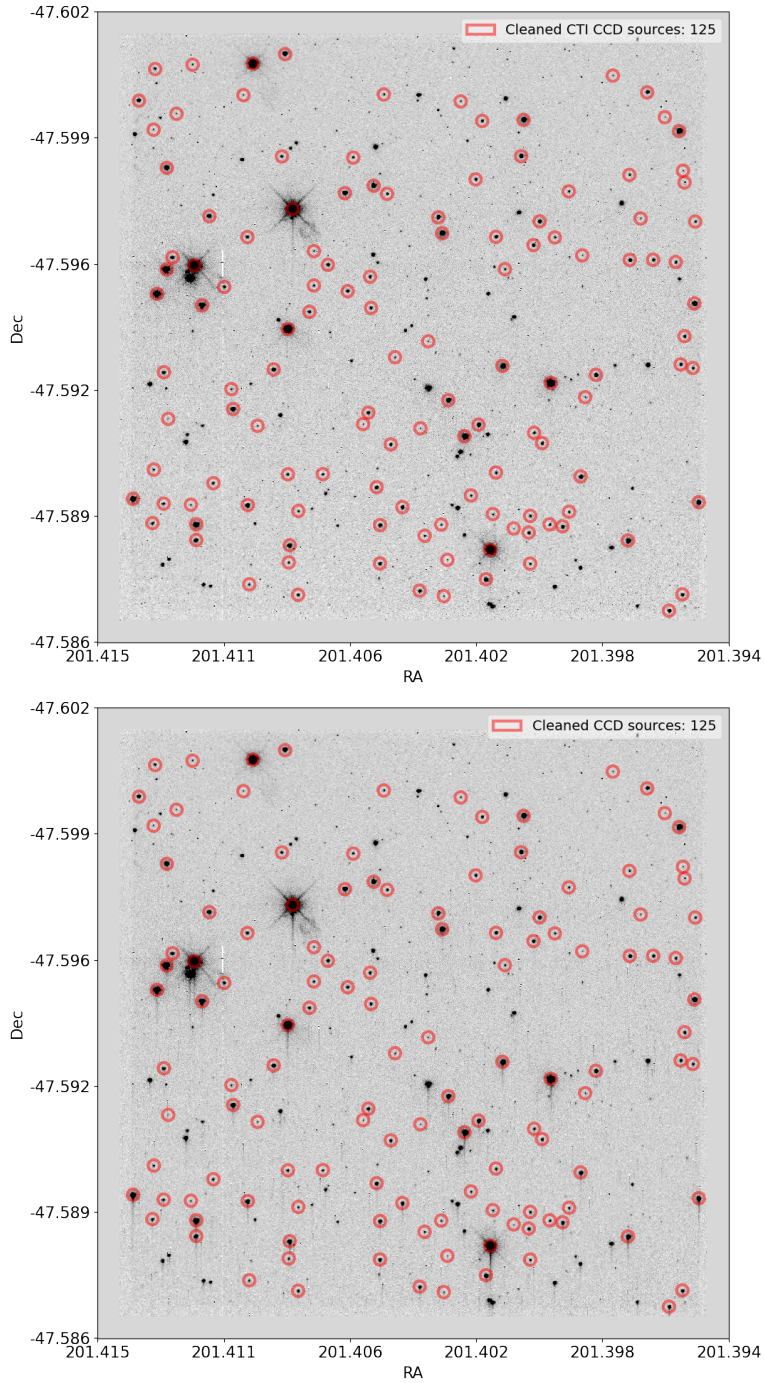


Figure 1. Cleaned list of 125 sources (red circles) identified on the pixel-based CTI corrected CCD reference image (ob01050) of NGC 5139 (top). Stars with close sources (within $0.8''$), contamination, or significant asymmetry were removed from the list. *Top:* Pixel-based CTI corrected image. *Bottom:* Non-CTI corrected image.

3.3 Photometry

To measure aperture photometry, we use tools from the PHOTUTILS package. To ensure a direct comparison of results between images (pixel-based CTI corrected and non-CTI corrected), we opt to use the same apertures (positions and size) across both. The aperture size used for each image is a radius $5 \times$ PSF FWHM as measured from the pixel-based CTI corrected images. The errors on the aperture photometry are determined using the error arrays of each image that include shot noise.

To determine a local sky background for every star, we define an annulus of inner radius of $5 \times$ PSF FWHM and thickness of 10 pixels for each. We create a rigorous sky mask for each source by making a low threshold (0.8) signal-to-noise ratio segmentation map. We take the sigma-clipped median of the unmasked sky pixels to determine accurate local sky values ($\sigma = 2$, no. iterations = 5) that are subtracted from the aperture pixels. The sky-subtracted net counts (NC) are measured for each source with the PHOTUTILS.APERTURE_PHOTOMETRY routine. The counts are converted to calibrated ST magnitudes (m) with the following equations.

$$m = -2.5 \times \log_{10}(F) + \text{PHOTZPT} \quad (1)$$

where

$$F = NC \times \text{PHOTFLAM} / \text{TEXPTIME}. \quad (2)$$

This relation uses keywords from the headers of each image: PHOTZPT (ST magnitude zeropoint), PHOTFLAM (inverse sensitivity in $\text{ergs/s/cm}^2/\text{\AA}$ per count/s), both populated by the PHOTCORR routine in the STIS pipeline from the IMPHTTAB reference file (5911632po_imp.fits), and TEXPTIME (total exposure time). An empirical CTI correction is then derived with the CTESTIS code and a Δm applied to the magnitudes derived from the non-CTI corrected images (see Section 2.2 for more details).

Figure 2 shows a plot of the ZMAG photometric parameter as a function of time. ZMAG is defined by the following equation that includes the photometric header keywords PHOTFLAM and PHOTZPT (as used in Equations 1 and 2).

$$\text{ZMAG} = -2.5 \times \log_{10}(\text{PHOTFLAM}) + \text{PHOTZPT}. \quad (3)$$

This parameter trends down with time and represents the change in photometric corrections. This decline is expected due to the natural degradation of the instrument's sensitivity. The change in ZMAG in post-SM4 data (12 years from 2010–2022) is -27.3 mmag which is a good measure of the TDS effects over this time period. The bump in ZMAG around MJD 57800 (2017) is observed in data processed with the previous IMPHTTAB (y2i1649no_imp.fits) as well as the new IMPHTTAB used here (5911632po_imp.fits). The bump arises in the PHOTFLAM header keyword and the origin is not clear, although we note in more recent years that the trend has smoothed.

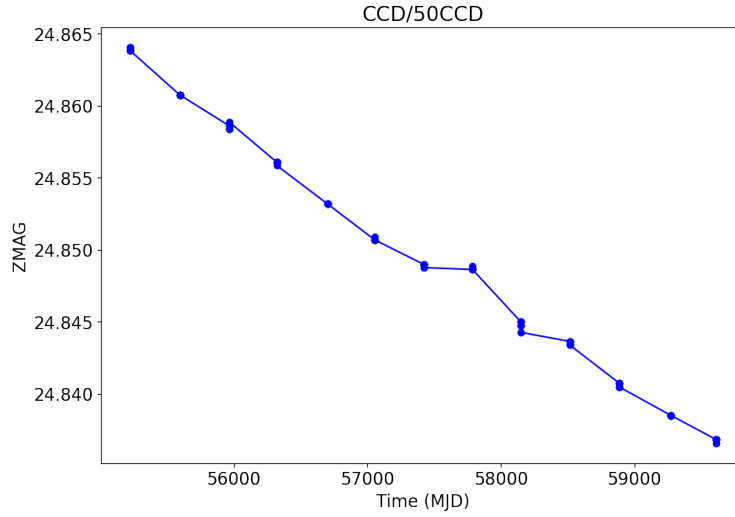


Figure 2. ZMAG photometric calibration as a function of time for the post-SM4 CCD data. ZMAG is derived using Equation 3 which includes the header keywords PHOTFLAM and PHOTZPT. The change in ZMAG in post-SM4 data (over 12 years) is -27.3 mmag which is a good reference for the effects of TDS over this period.

4. Results

4.1 CTI Corrected Magnitude Comparison

We first compare the CTI corrected magnitudes for the two methods, pixel-based and empirical, for each source on each image. Figure 3 shows the fractional difference between the magnitudes — $(\text{pixbased mag} - \text{empirical mag}) / \text{empirical mag}$ — as a function of pixel-based magnitude. A source with no magnitude difference between the two CTI methods would lie on the zero (horizontal) line. In the figure, the magnitude of each star measured across multiple images is represented by points of a single color and the median of those values is shown by the ‘X’s. Magnitude regions of interest are also highlighted on Figure 3 (gray dashed lines) for which we derive averages to compare our results to those presented in ISR 2015-04. A point above the line with a positive value means that the pixbased magnitude value is larger (i.e., the source is fainter) than the empirical correction, while a point below the line means the reverse is true. There is increased scatter for the fainter sources where these corrections become less reliable and CTI effects worsen.

For bright sources (< 18 mag), the pixbased and empirical CTI corrections are in good agreement, with an average offset of pixbased magnitudes being 0.020 mag fainter (0.12% difference). This is slightly larger than the average magnitude errors in this range (0.007 mag) but are ultimately very small. In the 18–19 mag range, the average difference increases with pixbased being 0.037 mag fainter than empirical (0.20% difference), and average magnitude errors of 0.023 mag. For the faintest range

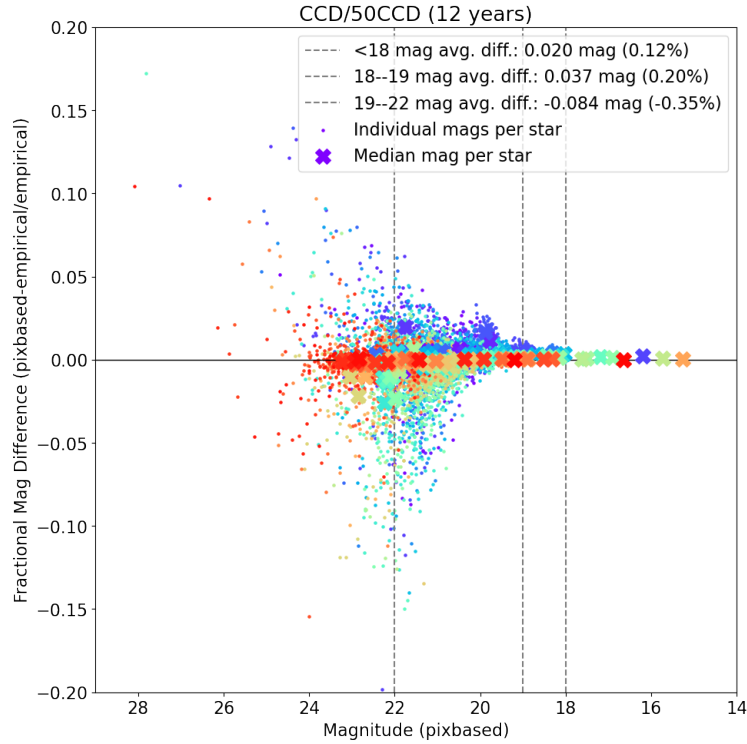


Figure 3. Fractional magnitude difference for the pixel-based CTI correction ('pixbased') and empirical Δm correction as a function of pixel-based magnitude. The zero (horizontal) line represents no difference between the CTI corrected magnitudes. Each color represents a single star, and each point is the magnitude measured for that star in different images. The median magnitude and fractional difference for each star is shown by the 'X' symbols of the same color. We show different magnitude ranges of interest (gray dashed lines) and the average magnitude and percentage differences for these ranges in the legend.

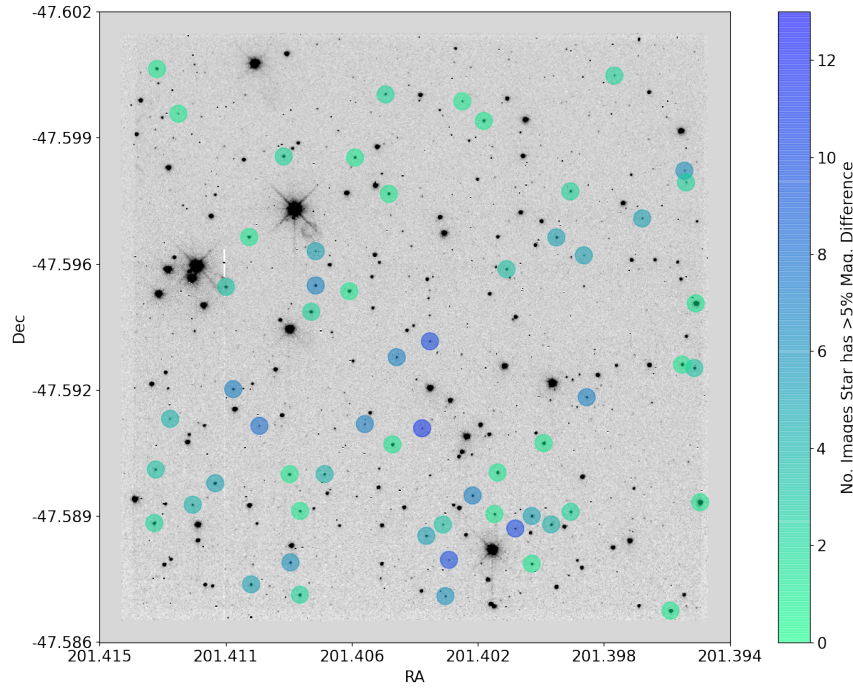


Figure 4. Spatial distribution of sources that have $> 5\%$ absolute magnitude difference between the two CTI correction methods (circles). The point colors indicate the number of images for which the source has an absolute magnitude discrepancy of $> 5\%$ (increasing green to blue). Sources towards the bottom of the image are more likely to have these larger discrepancies (more blue points) as the CTI effects worsen furthest from readout and for fainter sources.

from 19–22 mag, there is increased scatter and increased negative offset with pixbased being 0.084 mag brighter than empirical magnitudes (-0.35%). This offset is smaller than the average mag errors for this bin however (0.231 mag). We discuss these differences in more detail and compare them with ISR 2015-04 in Section 5.

4.2 Spatial Dependence of Outliers

We explore the spatial dependence of sources with large absolute offsets between the CTI corrected magnitudes. We define an outlier as those with an absolute magnitude difference of $> 5\%$ (i.e., > 0.05 or < -0.05 as shown on the fractional difference y -axis in Figure 3). As can be seen from Figure 3, these sources are all faint (mostly > 21 mag). We then count the number of images for which each source shows a greater than $> 5\%$ absolute magnitude difference. Of all the 65 CCD images used in this analysis, the highest number of images a source showed a $> 5\%$ magnitude difference was 13. All but one of the images with outliers are the shorter total exposure images (10 s) with reduced signal-to-noise per cosmic-ray split sub-exposure (2 s vs. 30 s).

Figure 4 shows the distribution of sources that show an absolute $> 5\%$ magnitude

offset (circles) in at least one image plotted on the pixel-based CTI corrected reference image (obat01050 of NGC 5139). The number of images that a source has this $> 5\%$ offset is color coded, increasing from green to blue (1–13). Sources toward the bottom of the image (i.e., furthest from the readout) are more prone to being outliers. CTI effects worsen furthest from the readout so this spatial dependence is expected. Reassuringly though, these $> 5\%$ outliers do not occur on all images or sources and represent a minority of derived magnitudes.

4.3 Time Dependence

The time dependence of the CTI effects is closely linked to, and degenerate with, the predicted TDS of the CCD detector. See ISR 2022-02 (updated analysis of ISR 2013-02) for a deeper look into the residual TDS trends for all three STIS detectors. We attempt to compare any time dependence in the CTI effects by looking at the same sources CTI corrected with the pixel-based and empirical methods, and those with no CTI correction. However, the CTI corrections themselves are correlated with the TDS trends of the detectors. Data observed at a 180-degree rotation could disentangle these two effects (see e.g., PID 14345 from ISR 2015-04). However, all the data analyzed here are at the same PA.

For each source we can track magnitude with time across the images. A correction for the effects of TDS is included in the CALSTIS pipeline using information from the IMPHTTAB reference file. Any magnitude trend with time measured from the sources is a residual time-dependence following this initial correction. Figure 5 shows example post-SM4 residual magnitude trends (after calibrations are applied) for a single star with no CTI correction (top), pixel-based CTI correction (middle) and the empirical CTI correction applied (bottom).

Inverse-variance weighted 1D polynomials are fitted to the data (green lines) to derive magnitude trends (mmag/year) for each source. The total exposure time of each image measurement is shown by the color scaling of the points (increasing green to blue). This is to show how the longer total exposure times affect the magnitudes and errors for each source. The longer 60 s exposures (blue points) show reduced scatter and smaller errors. We include the 10 s exposure throughout this analysis (as not included in ISR 2015-04) as they are mostly in good agreement and add to the statistical weight of the results.

As can be seen in Figure 5, there is a slight increased scatter in the magnitudes derived with the empirical CTI correction (as measured across all the individual stars). Prior to the CTI corrections, the stars show a positive magnitude trend which translates to the star appearing fainter with time (with the reverse magnitude scale). After the CTI corrections, the star appears brighter with time (negative trend) for both methods, with the trend being stronger for the empirical correction. However, the scatter for each individual star shows that the trend is consistent with zero within errors.

We derive these residual magnitude trends for each star and show histograms of

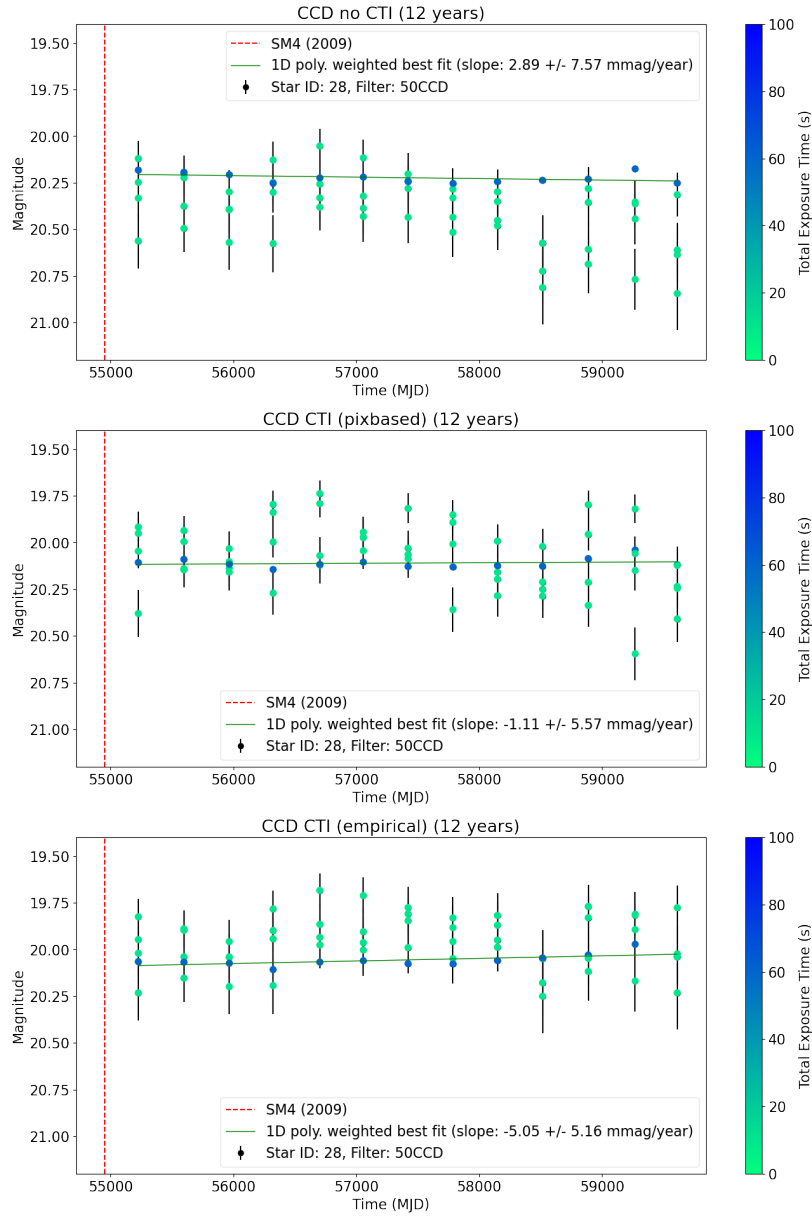


Figure 5. Example STIS CCD (50CCD filter) residual TDS trend plots as a function of time for a single star (ID 28, see Table 2). The SM4 timestamps (red dashed lines) and weighted 1D polynomial fits to the data (green lines) are shown. Points are color-coded with exposure time (increasing green to blue). *Top:* Non-CTI corrected magnitudes. *Middle:* Pixel-based CTI corrected magnitudes. *Bottom:* Empirically CTI corrected magnitudes.

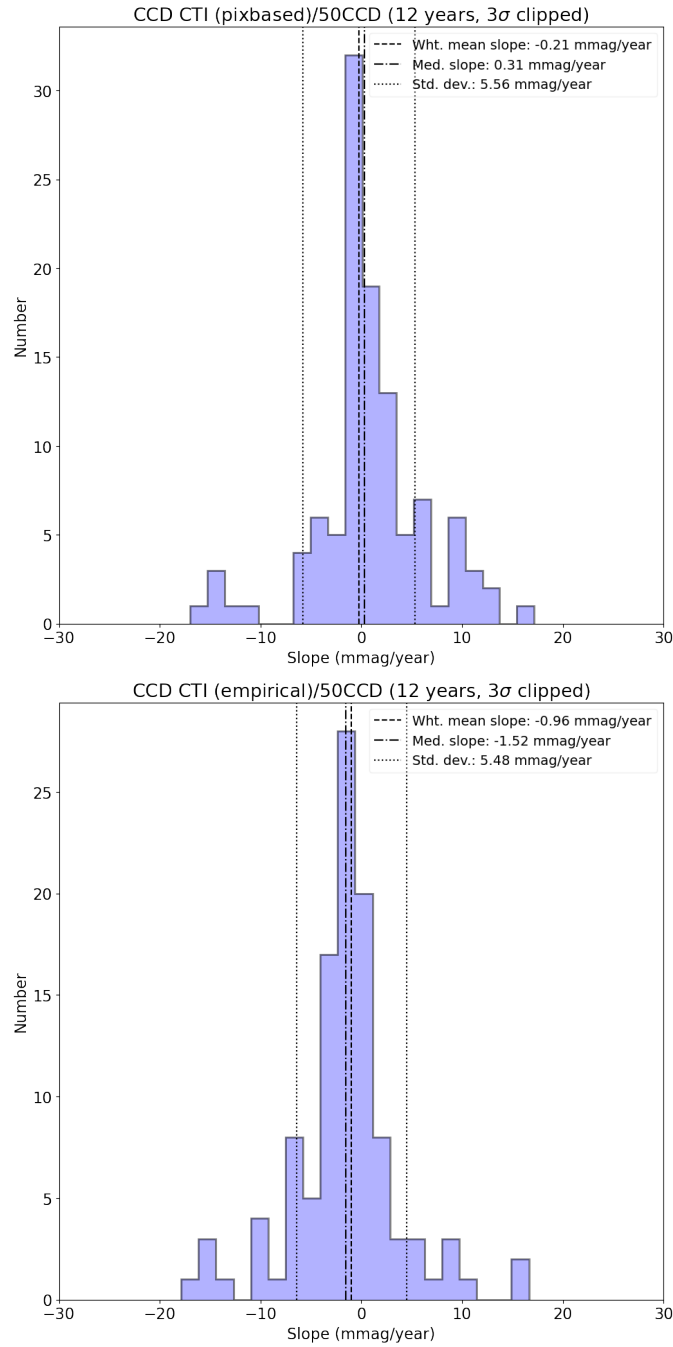


Figure 6. Sigma-clipped histograms of slopes derived from weighted 1D polynomial fits to the CCD data. The slopes have been 3 σ -clipped to remove extreme outliers (i.e., poorly fitted stars). The weighted mean (black dashed line), median (dot-dashed line), and standard deviation (dotted lines) of the clipped slope distribution are shown. *Top:* Slope distribution for the pixel-based CTI corrected magnitudes. *Bottom:* Slope distribution for the empirically CTI corrected magnitudes.

the resulting weighted slope fits in Figure 6. We perform 3σ -clipping to remove extreme outliers (i.e., poorly fitted stars) and measure statistics from the resulting sample of slopes. We see that the general trends observed for the individual star shown in Figure 5 hold for the full sample with a weighted mean slope of -0.21 ± 0.23 mmag/year (0.23% flux change) for the pixel-based correction and -0.96 ± 0.19 mmag/year (1.06% flux change) for the empirical CTI correction. For reference, the non-CTI magnitudes (histogram not shown) have average 0.34 ± 0.35 mmag/year (0.38% flux change). The pixel-based CTI correction and no CTI correction trends are consistent within errors to showing no trend with time, while the empirically CTI corrected magnitudes show a slight negative trend (stars appearing brighter with time). However, all these values are still consistent with the $\sim 1\%$ STIS flux calibration accuracy (e.g., Bohlin et al., 2019) and well within the $\sim 5\%$ quoted STIS photometric accuracy (STIS Instrument Handbook⁸).

4.4 Magnitude Dependence

We also explore how the derived residual magnitude trend slopes vary as a function magnitude. Figure 7 shows the slope (mmag/year) as a function of pixel-based magnitude for the non-CTI corrected (top panel, red), pixel-based CTI corrected (middle panel, green) and empirically CTI corrected (bottom panel, blue) stellar magnitudes. There is increased scatter for fainter magnitudes as expected. The median slope values are shown (gray dashed lines) with slightly positive slopes for non-CTI corrected magnitudes and slightly negative average slopes for the CTI corrected magnitudes.

To better compare the trends seen for each CTI correction method, we also display all three samples on Figure 8. We again show the non-CTI corrected (red), pixel-based corrected (green) and empirically CTI corrected (blue) slopes, this time binned by pixel-based magnitude. The number of stars in each bin is shown below their respective points and in the corresponding color for each sample. At fainter magnitudes, the corrections become less reliable (with absolute slope values increasing). Overall, the pixel-based CTI correction performs best at calibrating sources consistently with time (slopes closest to zero) with a marginal over correction of sources brighter than 19 mag (negative slopes, stars slightly brighter with time) and under correction (positive slopes, stars slightly fainter with time) for the sources fainter than 19 mag. Conversely, the empirical CTI correction consistently over-corrects the magnitudes for stars 15 to 23 mag.

⁸<https://hst-docs.stsci.edu/stisihb>

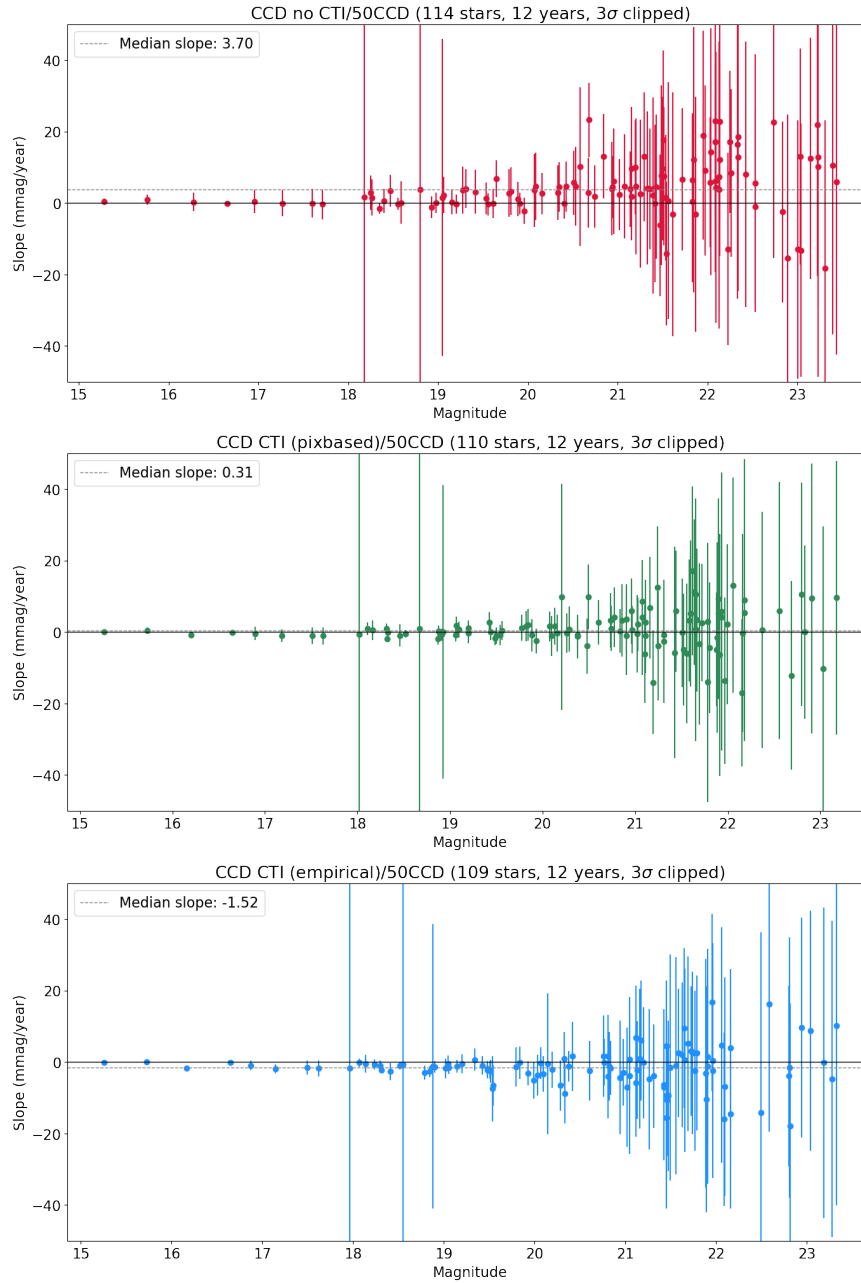


Figure 7. Residual TDS trend slopes (mmag/year) for individual stars as a function of stellar magnitude. See Figure 5 for examples of a trend plot and slope derived for a single star. *Top:* Slopes derived for non-CTI corrected magnitudes. *Middle:* Slopes derived for magnitudes measured from pixel-based CTI corrected images (STIS_CTI code). *Bottom:* Slopes derived for empirically CTI-corrected magnitudes.

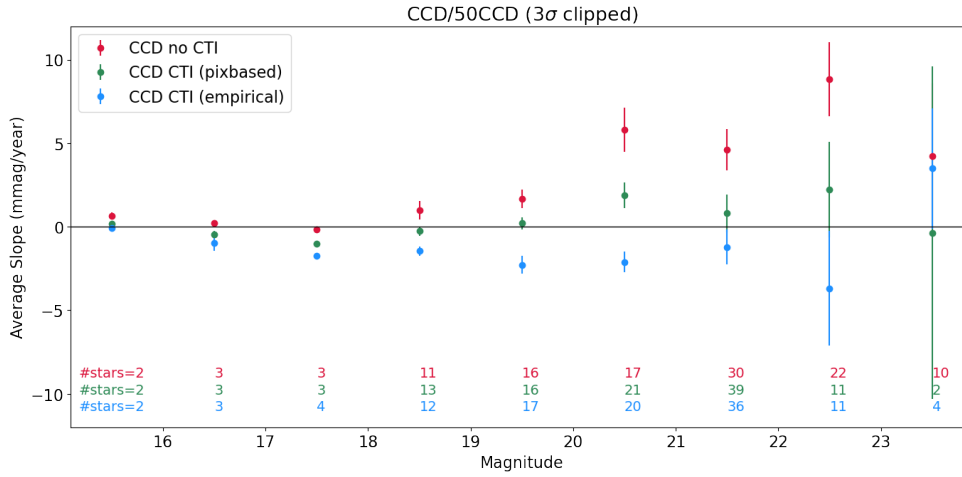


Figure 8. Residual TDS trend slopes (mmag/year) binned by stellar magnitude. Slopes derived for non-CTI corrected magnitudes (red), magnitudes measured from pixel-based CTI corrected images (green; STIS_CTI code) and empirically CTI corrected magnitudes (blue; CTESTIS code) are shown for comparison. The average slope per magnitude bin and number of stars averaged are shown below each point in the corresponding color. There are slightly different numbers of stars for each sample due to sigma clipping.

5. Discussion

5.1 Differences Between This Work and ISR 2015-04

The photometric accuracy of the two CTI correction methods, pixel-based and empirical, was previously tested in ISR 2015-04. We perform a separate analysis in this ISR to independently compare the two methods, and particularly the codes currently available to perform them. There are some important differences between the analysis presented here and that of ISR 2015-04 that we summarize here to provide context ahead of a direct comparison. We derive analogous statistics using the same ranges and similar plots to those presented in ISR 2015-04. However, we note that the differences in methods may be the main drivers of the numerical offsets and that the greater focus should be on the general observed trends.

The codes used in this work and ISR 2015-04 are based on the same principles and equations (e.g., Goudfrooij et al. 2006, Anderson & Bedin 2010) but were different than the codes now available for STIS (STIS_CTI for the pixel-based correction and CTESTIS for the empirical correction). In ISR 2015-04 an earlier version of the pixel-based CTI correction code with tunable parameters was adopted, with the advantage of being applicable to pre-SM4 data. The analysis in ISR 2015-04 did not use the empirical CTESTIS code from STISTOOLS, but rather an IDL routine based on the Goudfrooij et al. 2006 equations that was tested and found to have consistent (although not identical) results to the code used here.

It is unclear if the sky value used for the empirical correction in ISR 2015-04 is measured from non-sky subtracted images as required by the Goudfrooij et al. 2006 equations. Both ISR 2015-04 and ISR 2013-02 that used the empirical correction note a broad tail of negative slope values (corresponding to over-corrections). Upon testing the implementation of the CTESTIS code, this increased over-correction trend was also seen in this study when using local sky values measure around each star. We instead reverted to using the sky value measured from non-sky subtracted single sub-exposures (flt.fits) as recommended in Goudfrooij et al. 2006. A different implementation of this code may cause further discrepancies in a direct comparison.

The codes now available have gone through extensive testing, so we use these as they are most relevant for STIS users at present. We do not perform a detailed review of the code differences here but note that it may be the source of some additional discrepancies. We use a different range of data for this analysis (post SM4, from 2010 to 2022) as compared to ISR 2015-04 (1997 to 2015) as the pixel-based CTI correction code STIS_CTI is only properly calibrated for post-SM4 data at present. The images used for the previous CTI method comparison all had total exposure time ≥ 60 s. A comparison of results spanning the same time-window was therefore not performed as the ISR 2015-04 results included pre-SM4 data and only 60 s exposures. Additionally, ISR 2015-04 uses a similar but slightly different sample of 109 sources, compared to the results from 125 sources shown here.

The photometric methods presented in ISR 2015-04 were based on the IDL codes and methods of the full-field sensitivity analysis presented in ISR 2013-02. The full-field sensitivity analysis was updated and converted to Python routines in the new ISR 2022-02, and we use those same codes and analysis methods in this work. The methods are similar and comparable but not identical due to differences in the code, decisions for measuring photometry and different calibrations applied to STIS data between studies. It is also unclear from ISR 2015-04 if the aperture sizes used were of $5 \times$ PSF FWHM radius (as used in ISR 2013-02) or width of $5 \times$ PSF FWHM, which may produce slightly different magnitude values. They note good agreement with the ISR 2013-02 magnitudes (0.01–0.02 mag offsets), with any differences perhaps being explained in part by a potential difference in aperture size.

5.2 Comparison of Results

We compare the results between this work and that of ISR 2015-04 focusing mainly on the general trends rather than absolute values for the reasons noted in the previous section. For the brightest stars (< 18 mag) the CTI effects are small, and differences between the two correction methods are also minimal, found to be < 0.02 mag in ISR 2015-04 and this work. Between 18–19 mag the offsets were measured to be 0.02 mag near the detector center in ISR 2015-04 and 0.037 across the whole detector in this work. In ISR 2015-04, they find that for fainter magnitudes (19–22 mag) where CTI effects are larger, the empirical corrections over-correct the photometry while the pixel-based corrections under-correct the photometry, as also observed in this work including more

recent data.

ISR 2015-04 find that the histogram of slopes including data up to 2015 peak at slightly positive slopes (~ 1 mmag/year) as found in ISR 2013-02 and for data up to 2012 presented in ISR 2022-02. As presented in the recent full-field sensitivity analysis ISR 2022-02, including data up to 2022 caused a reversal of this trend from positive to negative for the CCD. This likely means that there is a slowdown in the sensitivity loss observed across the STIS modes, causing the previous calibrations to over-correct the data. Therefore, the slightly negative trends observed here are consistent with those general TDS detector changes seen when including more recent data. ISR 2015-04 also find relatively small offsets ($\sim 1\text{--}2$ mmag/year) between the peaks of the of the pixel-based and empirical slopes. In this work, we find even smaller offsets of 0.75 mmag/year between the empirical and pixel-based magnitude trend slopes, perhaps driven by the factors discussed previously.

6. Summary & Conclusions

In this work we compare two STIS CCD CTI correction methods, a pixel-based (STIS_CTI) and an empirical flux (CTESTIS) correction. The CTI corrections here are applied to data with two sky background levels (2 s and 30 s split exposure times). For the CTI method comparison, we use post-SM4 CCD data (spanning 2010 to 2022) and derive magnitudes for the same sources (within the same apertures) on both the pixel-based CTI corrected and non-CTI corrected images. We derive an empirical flux CTI correction for the magnitudes measured from the non-CTI corrected images with CTESTIS. We then perform analysis and compare results for non-CTI corrected magnitudes, pixel-based CTI corrected and empirically CTI corrected magnitudes.

We use the same alignment, source detection and photometry described in detail in the recent full-field sensitivity analysis in ISR 2022-02. We directly compare the derived CTI corrected magnitudes and explore any spatial dependence. We track the magnitudes as a function of time for each individual source and derive weighted slopes. We derive statistics to measure any residual TDS trend slopes for the stars with the different CTI corrections applied. We also explore how these derived slopes change as a function of magnitude. We suggest a possible avenue of investigation for future work for improving the time-dependence parameters of the pixel-based CTI code (STIS_CTI) in Appendix A.

Generally, the differences between the two CTI corrections are small ($\leq 1\%$) and well within the $\sim 5\%$ quoted STIS photometric accuracy. We note a number of differences between this work and the previous comparison presented in ISR 2015-04. However, the general trends between the two studies are consistent and the results of this work are summarized below.

1. For bright sources (< 18 mag) that are minimally affected by CTI, we find very close agreement between the CTI correction methods of 0.020 mag (0.12%)

difference). For slightly fainter sources (18–19 mag), we see a slightly increased average offset of 0.037 mag (0.2% difference). For faint sources (19–22 mag), we see more scatter and larger offsets of -0.084 mag (-0.35% difference) but within the average errors for this magnitude range (0.231 mag).

2. CTI effects are more severe furthest from the readout which results in a spatial dependence of sources more likely to have a $> 5\%$ absolute magnitude offset between the CTI correction methods.
3. For sources brighter than 19 mag, both CTI correction methods slightly over-correct the data, an effect that may be increasing with time. For sources fainter than 19 mag, the pixel-based CTI correction slightly under-corrects the stellar brightness (appearing fainter with time) while the empirical correction slightly over-corrects the stars (appearing brighter with time).
4. We find non-negligible residual time dependence following CTI corrections with both methods. The slopes derived for each of the exposure depths (2 s and 30 s per read) show similar trends for each CTI correction method and do not significantly impact a direct comparison of the two.
5. The pixel-based correction shows the most consistent correction with time (i.e., closest to no trend) and enables the most accurate CTI correction with more flexibility in its application than the empirically derived correction.

At present the empirical correction is the method that can be most easily applied to pre-SM4 data (with adequate calibration). Based on the results presented here, we recommend expanding the pixel-based correction to pre-SM4 data for increased accuracy across the full time period spanned by STIS CCD data.

Acknowledgments

Thanks to Sean Lockwood and Joleen Carlberg for reviewing this ISR and providing valuable insights and to the STIS team for valuable discussions that helped shape the analysis presented here. Thanks to Sean Lockwood and Paul Goudfrooij for helpful advice on implementing the CCD CTI corrections. Thanks also to Julia Roman-Duval for answering questions on the analysis presented in ISR 2013-02.

This research is based on observations made with the NASA/ESA *Hubble Space Telescope* obtained from the Space Telescope Science Institute. All of the data presented in this ISR were obtained from the Mikulski Archive for Space Telescopes (MAST). STScI is operated by the Association of Universities for Research in Astronomy, Inc., under NASA contract NAS5-26555.

References

- Anderson, J., & Bedin, L. R., 2010, PASP, 122, 895
- Astropy Collaboration et al., 2013, A&A 558, A33
- Astropy Collaboration et al., 2018, arXiv:1801.02634
- Biretta, J., Lockwood, S., & Debes J., 2015a, STIS Instrument Science Report 2015-03
- Biretta, J., Lockwood, S., & Debes J., 2015b, STIS Instrument Science Report 2015-04
- Biretta, J., Lockwood, S., & Debes J., 2015c, STIS Instrument Science Report 2015-05
- Bohlin, R., & Goudfrooij, P., 2003, STIS Instrument Science Report 2003-03
- Bohlin, R. C., Deustua, S. E., & de Rosa, G., 2019, AJ, 158, 5
- Bradley et al., 2020, Zenodo, astropy/photutils: 1.0.2
- Ginsburg, A., Sipocz, B. M., & Brasseur, C. E., et al., 2019, AJ, 157, 98
- Gonzaga, S., Hack, W., Fruchter, A., & Mack, J. 2012, The DrizzlePac Handbook (Baltimore, MD: STScI)
- Goudfrooij, P., & Bohlin, R., 2006, STIS Instrument Science Report 2006-03
- Goudfrooij, P., Bohlin, R. C., Maíz-Apellániz, J., & Kimble, R. A., 2006, PASP, 118, 848
- Hoffmann, S. L., Mack, J., et al. 2021, The DrizzlePac Handbook, Version 2.0 (Baltimore: STScI)
- Prichard, L., 2022a, STIS Instrument Science Report 2022-02
- Prichard, L., Welty, D. and Jones, A., et al. 2022 “STIS Instrument Handbook,” Version 21.0, (Baltimore: STScI)
- Roman-Duval, J., & Proffitt, C., 2013, STIS Instrument Science Report 2013-02

Appendix A

Future Work: Improving CTI Time Dependence Parameters

The effects of CTI worsen with time as exposure to radiation on orbit creates charge traps on the detector. Both CTI correction methods include time-dependent parameters to account for some of this degradation. It is valuable to be able to accurately model the effects of the CTI and TDS time-dependent components separately to improve calibration. However, it can be difficult to isolate the time-dependent effects of the CTI and TDS.

One potential approach is to look at CTI corrected and uncorrected net count rates where the TDS trends have not been removed. Comparing CTI-correction effects for images with different read times may allow us to start understanding its contribution for different exposure depths. Figure 9 shows sigma-clipped median ($\sigma = 3$, no. iterations = 5) net counts measured from non-CTI corrected images (red) and their corresponding pixel-based CTI corrected images (blue). We plot the sigma-clipped median source counts for each image as a function of time and fit inverse-variance weighted 1D polynomials. The two plots show median count trends for the two different

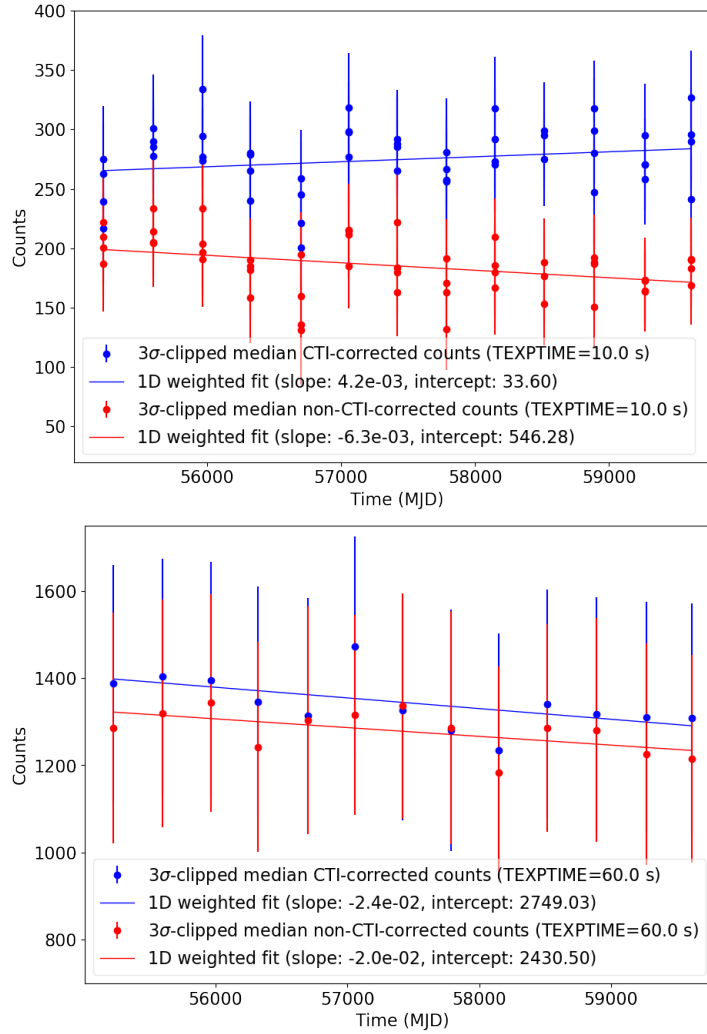


Figure 9. Sigma-clipped median net source counts measured from non-CTI corrected images (red) and corresponding pixel-based CTI-corrected images (blue). A 1D polynomial weighted fit (lines) is used to derive the slopes and intercepts. The combined TDS and CTI time-dependence trends are included in the slopes. *Top:* Counts comparison for 10 s exposures (2 s per read). *Bottom:* Counts comparison for 60 s exposures (30 s per read).

exposure times used here (10 s total, with 2 s per read and 60 s total, with 30 s per read).

The count measurements in Figure 9 are non-photometrically calibrated and therefore still include the uncorrected TDS trends. The derived slopes therefore show the TDS effects combined with the uncorrected CTI time-dependence (red slopes) and the TDS effects combined with any residual CTI time dependence following an initial correction (blue slopes). Each exposure depth shows a different slope following the CTI correction. Improving the time-dependent CTI parameters using these data is not possible since there is an exposure time dependence of the sky background level and we do not sample a large enough range to be able to constrain this relation.

Improving the time-dependence calibration of the pixel-based CTI code STIS_CTI could be investigated in the future with a larger data set than presented here. This could perhaps be performed by processing data with a wider range of exposure times with the pixel-based CTI code that does not include a CTI time-dependence correction (an all zero `SCALE` slope). Taking a ratio of the non-CTI corrected counts and zero-time dependence CTI corrected counts would cancel out any TDS effects to leave the absolute CTI time-dependence trend.

Appendix B

Table 1. STIS CCD exposures used in this analysis and their properties. The reference image is indicated with a † symbol.

Exposure	Program ID	Date of Observation	Exposure Time (s)	No. CR-splits CRSPLIT	Aperture /Amplifier	Orientation (PA_APER)	PSF FWHM (Moffat, pix)
obat01010	11854	2010-01-30	10.0	5	50CCD/D	-94.98	1.69
obat01020	11854	2010-01-30	10.0	5	50CCD/D	-94.98	1.65
obat01030	11854	2010-01-30	10.0	5	50CCD/D	-94.98	1.66
obat01040	11854	2010-01-30	10.0	5	50CCD/D	-94.98	1.62
obat01050†	11854	2010-01-30	60.0	2	50CCD/D	-94.98	1.69
obmj01010	12409	2011-02-05	10.0	5	50CCD/D	-94.98	1.55
obmj01020	12409	2011-02-05	10.0	5	50CCD/D	-94.98	1.59
obmj01030	12409	2011-02-05	10.0	5	50CCD/D	-94.98	1.59
obmj01040	12409	2011-02-05	10.0	5	50CCD/D	-94.98	1.54
obmj01050	12409	2011-02-05	60.0	2	50CCD/D	-94.98	1.69
obuo01010	12770	2012-02-09	10.0	5	50CCD/D	-94.98	1.62
obuo01020	12770	2012-02-09	10.0	5	50CCD/D	-94.98	1.61
obuo01030	12770	2012-02-09	10.0	5	50CCD/D	-94.98	1.65
obuo01040	12770	2012-02-09	10.0	5	50CCD/D	-94.98	1.69
obuo01050	12770	2012-02-10	60.0	2	50CCD/D	-94.98	1.71
oc5401010	13139	2013-01-31	10.0	5	50CCD/D	-94.98	1.65
oc5401020	13139	2013-01-31	10.0	5	50CCD/D	-94.98	1.61
oc5401030	13139	2013-01-31	10.0	5	50CCD/D	-94.98	1.66
oc5401040	13139	2013-01-31	10.0	5	50CCD/D	-94.98	1.72
oc5401050	13139	2013-01-31	60.0	2	50CCD/D	-94.98	1.71
ocfg01010	13542	2014-02-15	10.0	5	50CCD/D	-94.98	1.69
ocfg01020	13542	2014-02-15	10.0	5	50CCD/D	-94.98	1.66
ocfg01030	13542	2014-02-15	10.0	5	50CCD/D	-94.98	1.75
ocfg01040	13542	2014-02-15	10.0	5	50CCD/D	-94.98	1.65
ocfg01050	13542	2014-02-15	60.0	2	50CCD/D	-94.98	1.74
ocrj01010	13989	2015-02-04	10.0	5	50CCD/D	-94.98	1.82
ocrj01020	13989	2015-02-04	10.0	5	50CCD/D	-94.98	1.64
ocrj01030	13989	2015-02-04	10.0	5	50CCD/D	-94.98	1.72
ocrj01040	13989	2015-02-04	10.0	5	50CCD/D	-94.98	1.72
ocrj01050	13989	2015-02-04	60.0	2	50CCD/D	-94.98	1.81
od1r31010	14421	2016-02-03	10.0	5	50CCD/D	-94.98	1.77
od1r31020	14421	2016-02-03	10.0	5	50CCD/D	-94.98	1.69
od1r31030	14421	2016-02-03	10.0	5	50CCD/D	-94.98	1.79
od1r31040	14421	2016-02-03	10.0	5	50CCD/D	-94.98	1.72
od1r31050	14421	2016-02-03	60.0	2	50CCD/D	-94.98	1.75
odbc01010	14827	2017-02-02	10.0	5	50CCD/D	-94.98	1.63
odbc01020	14827	2017-02-02	10.0	5	50CCD/D	-94.98	1.47
odbc01030	14827	2017-02-02	10.0	5	50CCD/D	-94.98	1.59
odbc01040	14827	2017-02-02	10.0	5	50CCD/D	-94.98	1.57
odbc01050	14827	2017-02-03	60.0	2	50CCD/D	-94.98	1.67
odpf01010	14968	2018-01-30	10.0	5	50CCD/D	-94.98	1.67
odpf01020	14968	2018-01-30	10.0	5	50CCD/D	-94.98	1.57

Table 1. (cont'd)

Exposure	Program ID	Date of Observation	Exposure Time (s)	No. CR-splits CRSPLIT	Aperture /Amplifier	Orientation (PA_APER)	PSF FWHM (Moffat, pix)
odpf01030	14968	2018-01-30	10.0	5	50CCD/D	-94.98	1.60
odpf01040	14968	2018-01-30	10.0	5	50CCD/D	-94.98	1.69
odpf01050	14968	2018-01-30	60.0	2	50CCD/D	-94.98	1.68
odw401010	15556	2019-02-01	8.8	5	50CCD/D	-94.98	1.55
odw401020	15556	2019-02-01	10.0	5	50CCD/D	-94.98	1.68
odw401030	15556	2019-02-01	10.0	5	50CCD/D	-94.98	1.70
odw401040	15556	2019-02-01	10.0	5	50CCD/D	-94.98	1.63
odw401050	15556	2019-02-01	60.0	2	50CCD/D	-94.98	1.69
oe6801010	15745	2020-02-08	60.0	2	50CCD/D	-94.98	1.81
oe6801020	15745	2020-02-08	10.0	5	50CCD/D	-94.98	1.58
oe6801030	15745	2020-02-08	10.0	5	50CCD/D	-94.98	1.57
oe6801040	15745	2020-02-08	10.0	5	50CCD/D	-94.98	1.66
oe6801050	15745	2020-02-08	10.0	5	50CCD/D	-94.98	1.62
oeef01010	16347	2021-02-24	60.0	2	50CCD/D	-94.98	1.78
oeef01020	16347	2021-02-24	10.0	5	50CCD/D	-94.98	1.64
oeef01030	16347	2021-02-24	10.0	5	50CCD/D	-94.98	1.59
oeef01040	16347	2021-02-24	10.0	5	50CCD/D	-94.98	1.72
oeef01050	16347	2021-02-24	10.0	5	50CCD/D	-94.98	1.51
oelw01010	16555	2022-02-01	60.0	2	50CCD/D	-94.98	1.69
oelw01020	16555	2022-02-01	10.0	5	50CCD/D	-94.98	1.56
oelw01030	16555	2022-02-01	10.0	5	50CCD/D	-94.98	1.58
oelw01040	16555	2022-02-01	10.0	5	50CCD/D	-94.98	1.61
oelw01050	16555	2022-02-01	10.0	5	50CCD/D	-94.98	1.68

Table 2. The 125 cleaned sources identified from the pixel-based CTI corrected CCD reference image (obat1050) and used for analysis. x - and y -coordinates are the pixel coordinates on the reference image. The 19 stars stacked to create the PSF are indicated with a † symbol. Star ID 28 shown in Figure 5 is indicated with a * symbol.

Star ID	x -coordinate	y -coordinate	RA	Dec
1	995.9	54.7	201.415529	-47.599582
3	603.4	80.1	201.414292	-47.594099
4	349.5	82.4	201.413784	-47.590534
5	1019.2	83.1	201.414980	-47.599944
6	561.2	89.6	201.414017	-47.593518
10	264.2	100.6	201.413251	-47.589359
11	677.0	109.6	201.413809	-47.595168
15	492.1	137.0	201.412904	-47.592605
16	754.0	136.7	201.413383	-47.596283
17	332.9	138.9	201.412578	-47.590371
19	609.6	143.4	201.412984	-47.594263
21	684.4	161.0	201.412752	-47.595335
22	334.8	168.9	201.411957	-47.590433
23	924.4	177.1	201.412848	-47.598727
24	171.8	177.9	201.411475	-47.588154
25	570.0	185.3	201.412039	-47.593758
26	751.3	191.0	201.412247	-47.596311
27	725.2	198.1	201.412052	-47.595954
28*	810.2	201.8	201.412128	-47.597152
29	492.3	204.1	201.411507	-47.592689
30	171.9	205.4	201.410902	-47.588190
31	599.0	204.9	201.411683	-47.594188
32	787.9	205.2	201.412017	-47.596843
33	95.4	207.5	201.410721	-47.587117
34	753.9	220.0	201.411648	-47.596383
35	689.0	223.1	201.411465	-47.595475
36	821.8	227.2	201.411620	-47.597346
37	349.8	228.7	201.410738	-47.590717
39	531.2	235.3	201.410926	-47.593273
40	261.6	238.9	201.410366	-47.589491
42	162.5	239.6	201.410173	-47.588099
43	115.1	241.4	201.410050	-47.587435
44	1047.8	243.9	201.411679	-47.600541
45	61.5	249.8	201.409777	-47.586693
46	650.7	255.7	201.410719	-47.594977
49	486.3	270.1	201.410121	-47.592685
50	201.8	277.0	201.409464	-47.588696
52	841.8	288.9	201.410371	-47.597702
53	331.5	292.7	201.409371	-47.590538
54	392.6	292.9	201.409476	-47.591396
55	694.3	295.7	201.409963	-47.595637
56	98.0	300.9	201.408780	-47.587267
60	511.0	344.8	201.408609	-47.593123

Table 2. (cont'd)

Star ID	x -coordinate	y -coordinate	RA	Dec
61	774.8	347.1	201.409037	-47.596831
63	639.4	359.1	201.408543	-47.594944
66	760.8	365.1	201.408638	-47.596657
67	562.6	373.0	201.408116	-47.593882
68	278.7	377.1	201.407517	-47.589899
70	664.0	379.2	201.408167	-47.595314
71	462.8	380.2	201.407785	-47.592488
73	123.0	389.2	201.406983	-47.587726
74	471.8	400.2	201.407385	-47.592640
75	236.0	406.5	201.406828	-47.589335
76	611.2	421.7	201.407186	-47.594624
77	849.7	427.1	201.407504	-47.597982
78	233.1	441.2	201.406099	-47.589336
80	789.8	452.1	201.406876	-47.597170
83	868.5	466.1	201.406726	-47.598292
84	115.5	470.7	201.405274	-47.587719
85	306.9	475.7	201.405514	-47.590414
86	1037.6	478.1	201.406782	-47.600682
87	705.7	481.8	201.406106	-47.596024
88	1016.2	484.1	201.406617	-47.600389
89	518.3	496.9	201.405453	-47.593410
90	576.3	524.6	201.404979	-47.594259
91	1023.0	533.6	201.405598	-47.600545
92	331.5	546.2	201.404089	-47.590845
96†	369.2	576.1	201.403534	-47.591412
97	476.6	582.8	201.403587	-47.592928
98†	182.0	587.4	201.402961	-47.588796
99	1040.1	590.8	201.404436	-47.600855
101†	103.3	607.5	201.402401	-47.587714
102†	435.7	612.1	201.402905	-47.592391
103†	220.5	619.6	201.402359	-47.589376
104†	376.9	622.0	201.402592	-47.591576
105†	474.9	637.4	201.402448	-47.592972
106	120.4	650.0	201.401546	-47.588007
107	709.9	650.5	201.402599	-47.596289
108†	168.5	657.2	201.401484	-47.588691
109†	401.3	658.1	201.401882	-47.591963
111	1007.8	662.9	201.402876	-47.600489
112	927.5	666.7	201.402653	-47.599366
113	968.3	666.9	201.402721	-47.599939
115†	130.5	671.1	201.401124	-47.588174
117	844.8	674.6	201.402338	-47.598213
118	377.0	681.8	201.401345	-47.591650

Table 2. (cont'd)

Star ID	x -coordinate	y -coordinate	RA	Dec
119	759.8	692.5	201.401812	-47.597041
120	796.9	705.9	201.401600	-47.597579
121†	260.9	706.5	201.400622	-47.590049
122	694.4	706.9	201.401395	-47.596139
123†	600.4	713.1	201.401096	-47.594826
124	770.4	733.9	201.400968	-47.597240
125	1041.7	733.6	201.401464	-47.601051
127	946.5	739.0	201.401180	-47.599721
128	593.7	740.8	201.400507	-47.594766
129†	194.7	742.9	201.399744	-47.589163
130†	339.9	755.7	201.399738	-47.591219
132	504.6	781.9	201.399490	-47.593564
133†	431.0	783.0	201.399334	-47.592531
134	821.3	786.2	201.399971	-47.598018
136†	481.1	796.1	201.399152	-47.593251
137	1023.0	801.7	201.400011	-47.600872
138	658.9	807.1	201.399242	-47.595763
139	926.9	815.0	201.399561	-47.599537
140	1020.3	822.2	201.399578	-47.600857
141	120.6	827.3	201.397852	-47.588225
142†	445.6	845.1	201.398068	-47.592812
143†	321.2	847.1	201.397801	-47.591066
144	738.2	847.6	201.398542	-47.596926
148	1013.5	891.4	201.398124	-47.600847
149	97.5	893.7	201.396427	-47.587981
150	670.3	909.1	201.397138	-47.596047
151	742.4	910.9	201.397230	-47.597062
153	988.7	915.6	201.397575	-47.600527
154	137.4	921.6	201.395917	-47.588575
156	632.9	943.2	201.396360	-47.595562
157	72.0	944.4	201.395326	-47.587684
159	254.1	954.1	201.395451	-47.590254
160†	498.9	955.3	201.395866	-47.593694
161	958.0	959.0	201.396617	-47.600148
162	898.1	988.2	201.395899	-47.599342
163	100.1	999.6	201.394225	-47.588146
164	165.5	1007.1	201.394188	-47.589074
165	270.6	1009.0	201.394336	-47.590552
166	326.7	1025.6	201.394091	-47.591360